Many-body renormalization of forces in f-electron materials

Evgeny Plekhanov,[1,*] Phil Hasnip,[2] Vincent Sacksteder,[3] Matt Probert,[2] Stewart J. Clark,[4] Keith Refson,[3,5] and Cedric Weber[1]

[1]*King's College London, Theory and Simulation of Condensed Matter (TSCM), The Strand, London WC2R 2LS, United Kingdom*
[2]*Department of Physics, University of York, Heslington, York YO10 5DD, United Kingdom*
[3]*Department of Physics, Royal Holloway University of London, Egham, Surrey TW20 0EX, United Kingdom*
[4]*Department of Physics, University of Durham, Durham DH1 3LE, United Kingdom*
[5]*ISIS Facility, RAL, Chilton, Didcot OX11 0QX, United Kingdom*

We present the implementation of dynamical mean-field theory (DMFT) in the CASTEP *ab initio* code. We explain in detail the theoretical framework for DFT+DMFT and we demonstrate our implementation for three strongly-correlated systems with f-shell electrons: γ-cerium, cerium sesquioxide Ce_2O_3, and samarium telluride SmTe by using a Hubbard I solver. We find very good agreement with previous benchmark DFT+DMFT calculations of cerium compounds, while for SmTe we show the improved agreement with the experimental structural parameters as compared with LDA. Our implementation works equally well for both norm-conserving and ultrasoft pseudopotentials, and we apply it to the calculation of total energy, bulk modulus, equilibrium volumes, and internal forces in the two cerium compounds. In Ce_2O_3 we report a dramatic reduction of the internal forces acting on coordinates not constrained by unit cell symmetries. This reduction is induced by the many-body effects, which can only be captured at the DMFT level. In addition, we derive an alternative form for treating the high-frequency tails of the Green function in Matsubara frequency summations. Our treatment allows a reduction in the bias when calculating the correlation energies and occupation matrices to high precision.

I. INTRODUCTION

Density functional theory (DFT) is a key computational tool for modern material science, condensed matter physics, and solid-state chemistry [1–3]. It can treat an immense range of materials, including bulk metals, oxides, semiconductors, graphene and layered materials, and surfaces. Practical DFT calculations, however, rely on approximate exchange-correlation functionals, which handicaps the ability of DFT to reproduce strongly correlated physics in many materials, notably those containing open d- or f-shell elements. Many strongly-correlated materials exhibit properties useful for technological applications [4–6]. For example, the copper oxides and iron pnictides are high temperature superconductors [7–9], and the cobaltates exhibit colossal thermoelectric power [10] which is useful for energy conversion. Several vanadates have peculiar room-temperature metal-insulator transitions, allowing realization of a so-called "intelligent window," which becomes insulating as the external temperature drops [11–14]. The failure of DFT's exchange-correlation functionals to capture strong correlation physics severely limits its use for nanoscale design of these many important functional materials.

In contrast to DFT, huge progress has been made in describing strongly-correlated materials with dynamical mean-field theory (DMFT) [15–20]. DMFT is a sophisticated method which offers a higher level of theoretical description than DFT and bridges the gap between DFT and Green function approaches. Within DMFT, the treatment of local electronic correlation effects is formally exact, although the nonlocal electronic correlation effects are neglected.

In this paper, we provide a fast and stable implementation of the full charge self-consistent DFT+DMFT method in the widely used plane-wave DFT code CASTEP [1,2,21,22] and benchmark this implementation by calculating spectral properties, energetics, and forces for γ-Ce, Ce_2O_3, and SmTe. It was shown previously [20] that full charge self-consistency is not crucial for these compounds and the Hubbard I solver (at least at the level of total energy). Therefore, in this paper, we focus on the DMFT approach within the framework of fixed Kohn-Sham (KS) potentials, the so-called "one-shot" DFT+DMFT method. We show that our predicted equilibrium volume and bulk modulus for cerium compounds are in excellent agreement with the existing literature, i.e., that taking into account strong correlations improves the agreement with the experiment compared to DFT. Moreover, by calculating the atomic forces in cerium sesquioxide we show that DFT overestimates them by almost a factor of two.

The rest of this paper is organized as follows: In Sec. II, we rederive the DFT+DMFT formalism in the case of plane-wave basis; in Secs. III and IV, we illustrate our results on the examples of γ-Ce and cerium sesquioxide; finally Sec. V is dedicated to the conclusions.

II. METHODS

A. General formalism

There exist in the literature several proposals for combining DFT and DMFT [20,23–26]. Here, we follow closely the DFT+DMFT formulation proposed in Refs. [20,23].

*evgeny.plekhanov@kcl.ac.uk

Nevertheless, in contrast with Ref. [20], where an LMTO basis was considered, we deal with a plane-wave code CASTEP. On the other hand, contrarily to Ref. [23], we use a different orthogonalization procedure. We therefore, rederive all the formulas relevant for our case taking into account these differences.

The total energy functional was derived in Refs. [17,19,20] and is reported here for completeness. The starting point is the Baym-Kadanoff (or Luttinger-Ward) functional (for a review see Ref. [19]), which is a functional of electronic density $\rho(\mathbf{r})$ and an impurity Green function $G_{m,m'}^{\mathbf{R}}(i\omega_n)$ with the respective constraint fields $v_{KS}(\mathbf{r})$ and $\Sigma_{m,m'}^{\mathbf{R}}(i\omega_n)$:

$$\Omega[\rho, G_{m,m'}|v_{KS}, \Sigma_{m,m'}]$$
$$= \operatorname{Tr} \ln \hat{G} - \int d\mathbf{r}(v_{KS}(\mathbf{r}) - v_c(\mathbf{r}))\rho(\mathbf{r}) - \operatorname{Tr} G\Sigma$$
$$+ \frac{1}{2} \int d\mathbf{r}d\mathbf{r}'\rho(\mathbf{r})\frac{1}{|\mathbf{r} - \mathbf{r}'|}\rho(\mathbf{r}') + E_{xc}[\rho]$$
$$+ \sum_{\mathbf{R}} \left(\Phi_{\text{imp}}[G_{m,m'}^{\mathbf{R}}] - \Phi_{DC}[G_{m,m'}^{\mathbf{R}}]\right). \tag{2.1}$$

Here, $G_{m,m'}^{\mathbf{R}}(i\omega_n)$ and $\Sigma_{m,m'}^{\mathbf{R}}(i\omega_n)$ are defined as matrices in orbital indices m and m' and functions of Matsubara frequencies $i\omega_n$, $E_{xc}[\rho]$ is the exchange-correlation functional, $v_c(\mathbf{r})$ is the periodic potential of the ions, $\Phi_{\text{imp}}[G_{m,m'}^{\mathbf{R}}]$ is the DMFT interaction functional, and $\Phi_{DC}[G_{m,m'}^{\mathbf{R}}]$ is the double-counting functional. Finally, $\hat{G}$ is the Bloch Green function operator:

$$\hat{G}(\mathbf{r}, i\omega_n) = \left(i\omega_n + \mu + \tfrac{1}{2}\nabla^2 - v_{KS}(\mathbf{r}) - \Sigma^B(\mathbf{r}, i\omega_n)\right)^{-1}. \tag{2.2}$$

$\Sigma^B(\mathbf{r}, i\omega_n)$ is the Bloch self-energy obtained by up-folding of $\Sigma_{m,m'}^{\mathbf{R}}$ (explained below), while $\operatorname{Tr} A$ of a matrix function (or operator) is the shorthand notation for:

$$\operatorname{Tr} A = T \sum_{n,l} A_{ll}(i\omega_n)e^{i\omega_n 0^+}, \tag{2.3}$$

i.e., traced over both orbital and imaginary time indices at temperature T. Here, we use the atomic Hartree units, so that $\hbar = 1$, $e = 1$, and $m_e = 1$. The variation of Ω with respect to ρ and $G_{m,m'}^{\mathbf{R}}$ gives the constraint potentials v_{KS} and $\Sigma_{m,m'}^{\mathbf{R}}$ respectively:

$$v_{KS}(\mathbf{r}) = v_c(\mathbf{r}) + \frac{\delta E_{xc}}{\delta\rho} + \int d\mathbf{r}'\frac{1}{|\mathbf{r} - \mathbf{r}'|}\rho(\mathbf{r}')$$
$$\Sigma_{m,m'}^{\mathbf{R}} = \frac{\delta\Phi_{\text{imp}}}{\delta G_{m,m'}^{\mathbf{R}}} - V^{DC}. \tag{2.4}$$

Here V_{DC} is the double counting potential:

$$V^{DC} = \frac{\delta\Phi_{DC}[G_{m,m'}^{\mathbf{R}}]}{\delta G_{m,m'}^{\mathbf{R}}}, \tag{2.5}$$

while the variation of Φ_{imp} with respect to $G_{m,m'}^{\mathbf{R}}$ is by construction the outcome of the impurity solver—the impurity self-energy:

$$\frac{\delta\Phi_{\text{imp}}[G_{m,m'}^{\mathbf{R}}]}{\delta G_{m,m'}^{\mathbf{R}}} = \Sigma_{m,m'}^{\text{imp}}. \tag{2.6}$$

On the other hand, the variation with respect to v_{KS} and $\Sigma_{m,m'}^{\mathbf{R}}$, taking into account (2.4), yields ρ and $G_{m,m'}^{\mathbf{R}}$, respectively:

$$\rho(\mathbf{r}) = \operatorname{Tr}\langle\mathbf{r}|\hat{G}|\mathbf{r}\rangle$$
$$G_{m,m'}^{\mathbf{R}} = \langle\chi_{m\mathbf{R}}|\hat{G}|\chi_{m'\mathbf{0}}\rangle, \tag{2.7}$$

where $\{\chi_{m\mathbf{R}}\}$ is the localized basis, used to define the Coulomb interaction. Here indices $m\mathbf{R}$ signify mth orbital on ion sitting at position $\mathbf{R}$. We will also use in what follows an abbreviated notation including spin notation σ: $\{m\mathbf{R}\sigma\} = L$. From (2.4), the constraint field v_{KS} and $\Sigma_{m,m'}$ can be expressed in terms of ρ and $G_{m,m'}^{\mathbf{R}}$. We thus arrive at the functional Γ, which is a functional of only ρ and $G_{m,m'}^{\mathbf{R}}$:

$$\Gamma[\rho, G_{m,m'}^{\mathbf{R}}] = \Omega[\rho, G_{m,m'}^{\mathbf{R}}|v_{KS}[\rho], \Sigma_{m,m'}^{\mathbf{R}}[G_{m,m'}^{\mathbf{R}}]]. \tag{2.8}$$

Finally, the minimum free energy is obtained by noting that at minimum [19] $\Gamma[\rho, G_{m,m'}^{\mathbf{R}}] = F[\rho, G_{m,m'}^{\mathbf{R}}]$. Thus, substituting ρ and $G_{m,m'}^{\mathbf{R}}$ and (2.4) into (2.1) gives the minimal value of the free energy. At zero temperature, the free energy reduces to the total (internal) energy, which can be rewritten using the DFT total energy [20]:

$$E_{\text{tot}} = E_{\text{DFT}} - \sum_{\nu,\mathbf{k}} f_\nu^{DFT}(\mathbf{k})\varepsilon_{\mathbf{k},\nu}^{DFT}$$
$$+ \sum_{\nu,\mathbf{k}} N_{\nu,\nu}(\mathbf{k})\varepsilon_{\mathbf{k},\nu} + E_U - E^{DC}. \tag{2.9}$$

Here k is the crystal momentum, ν is the band index, E_{DFT} is the total energy of underlying DFT calculations, $f_\nu^{DFT}(\mathbf{k})$ and $N_{\nu,\nu'}(\mathbf{k})$ are the DFT and DMFT (defined below) occupation matrices, respectively, $\varepsilon_{\mathbf{k},\nu}$ is the eigenspectrum of the KS Hamiltonian with the density, corrected by DMFT (in one-shot DFT+DMFT: $\varepsilon_{\mathbf{k},\nu} = \varepsilon_{\mathbf{k},\nu}^{DFT}$). E^{DC} is the double counting energy (defined in different approximations in Appendix B), while E_U is the DMFT correlation energy, which can be either calculated directly from the solver, as the average of the interaction term, or via Galitskii-Migdal formula [27]:

$$E_U = \frac{1}{2} \sum_{\mathbf{R}} \operatorname{Tr}[G^{\mathbf{R}}(i\omega_n)\Sigma^{\mathbf{R}}(i\omega_n)]. \tag{2.10}$$

By using a separation into a low-frequency numeric part and an analytic sum of high-frequency tails, this summation can be accomplished efficiently. We use a slightly modified version of the summation as explained in Appendix C.

Up to this point we did not specify the form of the localized basis $|\chi_{m\mathbf{R}}\rangle$ and the formalism remained general. In CASTEP, we use an already implemented LCAO basis, with the radial part derived from pseudopotential [28], which can be either norm-conserving or ultrasoft. In the case of norm-conserving pseudopotentials, the states $|\chi_{m\mathbf{R}}\rangle$ are orthogonal by construction, while in the case of ultrasoft ones [29] these states are overlapping with an overlap matrix S:

$$\langle\chi_{m'\mathbf{R}'}|\hat{S}|\chi_{m\mathbf{R}}\rangle = \delta_{m',m}.$$

This implies that the KS equation transforms from a standard eigenvalue problem into a generalized one:

$$\hat{H}_k^{KS}|\Psi_{\mathbf{k},\nu}\rangle = E_{\mathbf{k},\nu}\hat{S}|\Psi_{\mathbf{k},\nu}\rangle,$$

where we have introduced the KS eigenstates $|\Psi_{\mathbf{k},\nu}\rangle$. The two cases (norm-conserving and ultrasoft pseudopotentials) can be unified by defining an overlap matrix in the norm-conserving case to be identity matrix. In what follows, we will present the general formalism, valid for both norm-conserving and ultrasoft pseudopotentials used in CASTEP. It will become clear from what follows that the whole formalism does not depend on S, provided that all the scalar products are defined using S as a metric. Next, we define the projectors $P_{L,\nu}(\mathbf{k})$:

$$P_{L,\nu}(\mathbf{k}) = \langle \chi_L | S | \Psi_{\mathbf{k},\nu} \rangle. \qquad (2.11)$$

$P_{L,\nu}(\mathbf{k})$ are S orthonormal to a high degree (in both systems considered here the spilling factor was of the order of 0.1%). In order to ensure the full S orthogonality, we apply Löwdin orthogonalization procedure in the S-metric space. From now on, we have two bases, spanning two different spaces: (i) Bloch space (indexed by $\mathbf{k}$, ν) and (ii) localized basis or "correlated" subspace (indexed by L). The two spaces are connected by the projection procedure, also called up-folding (to go from χ_L to $\Psi_{\mathbf{k},\nu}$):

$$|a_{\mathbf{k},\nu}\rangle = \sum_L P^\star_{\nu,L}(\mathbf{k})|b_L\rangle \qquad (2.12)$$

or down-folding (vice versa):

$$|b_L\rangle = \sum_{\mathbf{k},\nu} P_{L,\nu}(\mathbf{k})|a_{\mathbf{k},\nu}\rangle. \qquad (2.13)$$

Here $|a_{\mathbf{k},\nu}\rangle$ is a vector living in the Bloch space and $|b_L\rangle$ is a vector defined in the space of "correlated" orbitals. For the current implementation it is only important to have localized basis states on the "correlated" orbitals. The matrix $P_{L,\nu}(\mathbf{k})$ is, in general, a complex rectangular matrix, satisfying the following condition:

$$\sum_{k,\nu} P_{L,\nu}(\mathbf{k}) P^\star_{\nu,L'}(\mathbf{k}) = \delta_{L,L'}. \qquad (2.14)$$

This condition is a consequence of completeness and S orthogonality of the KS eigenbasis, and the S orthogonality (after Löwdin orthogonalization) of the "correlated" orbitals. Because both Bloch and "correlated" spaces have the same metric, up- and down-folding are accomplished "as if there were no metric at all." An important consequence of this property stays in the fact that an up-folding followed by a down-folding is an identity operation (in the "correlated" space), which guarantees that during DMFT iterations the charge is conserved.

In the Bloch space the Bloch (or lattice) Green function can be obtained from (2.2) by taking the average over KS states $|\Psi_{\mathbf{k},\nu}\rangle$. On the other hand, G^B is a Fourier transform of $\langle \mathbf{r} | \hat{G} | \mathbf{r} \rangle$ into reciprocal space. In reciprocal space it takes the following form:

$$
\begin{aligned}
G^B_{\nu,\nu'}(\mathbf{k}, i\omega_n) &= ((i\omega_n + \mu - \varepsilon_{\kappa,\nu})\delta_{\nu,\nu'} - \Sigma^B_{\nu,\nu'}(\mathbf{k}, i\omega_n))^{-1} \\
&= \text{F.T.}[\langle \mathbf{R} | \hat{G} | \mathbf{0} \rangle].
\end{aligned} \qquad (2.15)
$$

Let us consider a correlated atom at position $\mathbf{R}$. The basis functions in its "correlated space" are enumerated by index m. As prescribed by the DMFT methodology, the local Green function at that site is obtained from the Bloch one by down-folding and summation over the Brillouin zone:

$$G^{\text{loc}}_{m,m'}(i\omega_n) = \frac{1}{N_{\mathbf{k}}} \sum_{\nu,\nu',\mathbf{k}} P_{m,\nu}(\mathbf{k}) G^B_{\nu,\nu'}(\mathbf{k}, i\omega_n) P^\star_{\nu',m'}(\mathbf{k}). \qquad (2.16)$$

On the other hand, within the on-site Anderson impurity problem, Dyson equation relates G^{imp}, Σ^{imp}, and the Weiss field $\mathscr{G}_0$:

$$[\mathscr{G}_0(i\omega_n)]^{-1}_{m,m'} = \Sigma^{\text{imp}}_{m,m'}(i\omega_n) + [G^{\text{imp}}(i\omega_n)]^{-1}_{m,m'}. \qquad (2.17)$$

The above equation serves as a definition for $\mathscr{G}_0$ by making the fundamental DMFT assumption: $G^{\text{imp}} = G^{\text{loc}}$ (and $\Sigma^{\text{imp}} = \Sigma^{\text{loc}}$). $\mathscr{G}_0$ will be used by the impurity solver in the next step. Alternatively, one can use the hybridization $\Delta(i\omega_n)$ instead of $\mathscr{G}_0$:

$$\Delta_{m,m'}(i\omega_n) = i\omega_n - \epsilon_{m,m'} + \mu - [\mathscr{G}_0(i\omega_n)]^{-1}_{m,m'}. \qquad (2.18)$$

Here $\epsilon_{m,m'}$ is the local impurity energy matrix, obtained by down-folding the KS Hamiltonian onto "correlated space" of the given correlated atom:

$$\epsilon_{m,m'} = \frac{1}{N_{\mathbf{k}}} \sum_{\mathbf{k},\nu} P_{m,\nu}(\mathbf{k}) \varepsilon^{KS}_{k,\nu} P^\star_{\nu,m'}(\mathbf{k}). \qquad (2.19)$$

The outcome of the impurity solver is the new impurity self-energy denoted as $\Sigma^{\text{imp}}_{m,m'}(i\omega_n)$. It is subsequently up-folded into the Bloch subspace (after the subtraction of the double-counting corrections $V^{DC}_{m,m'}$):

$$\Sigma^B_{\nu,\nu'}(\mathbf{k}, i\omega_n) = P^\star_{\nu,m}(\mathbf{k})\big(\Sigma^{\text{imp}}_{m,m'}(i\omega_n) - V^{DC}_{m,m'}\big)P_{m',\nu'}(\mathbf{k}). \qquad (2.20)$$

Thus up-folded Bloch self-energy acquires k dependence. Σ^B is then inserted into (2.15) and the calculations proceed until the convergence on chemical potential and self-energy is reached with a given tolerance.

At convergence, the system's properties can be evaluated: total energy from (2.9), and, in principle, any single particle properties from the Bloch Green function. For example, the DFT+DMFT occupation matrix $N_{\nu,\nu'}(k)$ (which is not diagonal, unlike in conventional DFT) is obtained from $G^B_{\nu,\nu'}(\mathbf{k}, i\omega_n)$ as:

$$N_{\nu,\nu'}(\mathbf{k}) = T \sum_n G^B_{\nu,\nu'}(\mathbf{k}, i\omega_n) e^{i\omega_n 0^+}, \qquad (2.21)$$

and hence the total number of electrons in the unit cell, used to fix the chemical potential μ, is given by:

$$N_e = \frac{1}{N_{\mathbf{k}}} \sum_{\nu,\mathbf{k}} N_{\nu,\nu}(\mathbf{k}). \qquad (2.22)$$

The spectral density $A(\mathbf{k}, \omega)$ (in real frequency) is derived from analytically continued (see details in the next subsection) G^B as:

$$A_{\nu,\nu}(\mathbf{k}, \omega) = -\frac{1}{\pi} \text{Im} G^B_{\nu,\nu}(\mathbf{k}, \omega), \qquad (2.23)$$
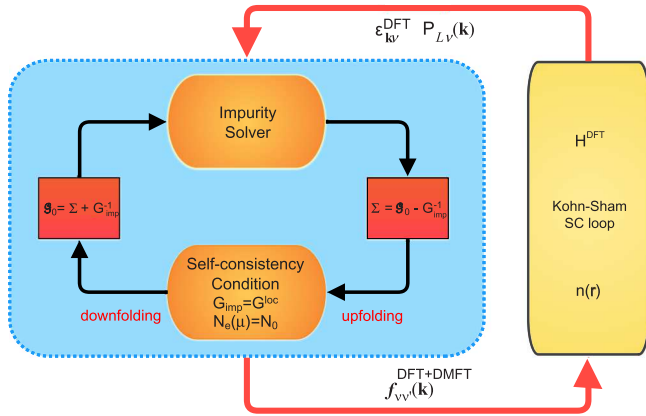
FIG. 1. DFT+DMFT execution flowchart, containing both the inner self-consistency loop (DMFT at fixed charge density) as well as the outer one (Kohn-Sham equations at DFT+DMFT charge density).

while the total DOS $D(\omega)$ is in turn obtained from $A_{\nu,\nu}(\mathbf{k}, \omega)$ by integrating over the Brillouin zone:

$$D(\omega) = \frac{1}{N_k} \sum_{k,\nu} A_{\nu,\nu}(\mathbf{k}, \omega). \qquad (2.24)$$

One can also calculate the partial DOS derived from the impurity Green function:

$$D_{\mathrm{imp}}(\omega) = -\frac{1}{\pi} \sum_m \mathrm{Im} G_{m,m}^{\mathrm{imp}}(\omega). \qquad (2.25)$$

To conclude this subsection, we summarize the program workflow. The execution proceeds as follows:

(i) The electronic density is converged at the DFT level.

(ii) An initial guess for self-energy $\Sigma_{m,m'}^{\mathbf{R}}$ is made, which is subsequently up-folded into Bloch space: Σ^B.

(iii) Chemical potential μ is determined at fixed Σ^B.

(iv) $\mathscr{G}_0(i\omega_n)$ [or $\Delta(i\omega_n)$] is formed by down-folding G^B.

(v) Call of impurity solver updates $\Sigma_{m,m'}^{\mathbf{R}}$.

(vi) Up-folding $\Sigma_{m,m'}^{\mathbf{R}}$ gives new Σ^B.

(vii) If the convergence for μ and Σ^B is not reached, go to (iii).

(viii) If full charge self-consistency is requested, update the charge density $n(\mathbf{r})$ and go to (i).

(ix) Compute system's properties within DMFT.

This workflow is illustrated in Fig. 1.

B. Solvers

It is evident from the previous subsection that the central point of DMFT method is the solution of the impurity problem. This is normally accomplished by the so-called impurity solver. Several methods have been developed in the past. At present, we implement in CASTEP three impurity solvers:

(i) Hubbard I (see, e.g., Refs. [20,30]).

(ii) Continuous time quantum Monte Carlo with hybridization expansion CT-HYB available through TRIQS package [31].

(iii) Exact diagonalization with cluster perturbation theory (ED-CPT) solver [32].

Each of these solvers has its advantages and deficiencies which we list shortly below. Within Hubbard I approximation the impurity is treated as an isolated atom (atomic limit) and the hybridization with the bath is totally neglected. The Weiss field in Hubbard I can be expressed as: $\mathscr{G}_0^{-1} = i\omega_n + \mu - \epsilon$. Of course, such an approximation is very crude, but might be acceptable for strongly localized orbitals (e.g., f shells in rare-earth elements). Moreover, an important advantage of Hubbard I consists in its ability to work on both real and imaginary frequency axes, allowing analytic continuation to be avoided. Finally, it is fast and free from statistical bias, which allows us to use it for quick tests and for total energy and forces calculations.

In contrast to the Hubbard I method, in the case of density-density only interactions, a CT-HYB solver offers a numerically exact solution to the impurity problem with a given Weiss field $\mathscr{G}_0(i\omega_n)$ at a reasonable computational cost. As is evident from its name, CT-HYB builds its perturbation expansion in powers of hybridization and therefore could require more resources in the case of a strongly hybridized impurity. The output of CT-HYB solver is the self-energy in imaginary frequency, which means that some routine for analytic continuation is needed to obtain the real-axis results. In CASTEP, we use the Pade approximation [33] with the calculations using arbitrary precision arithmetic [34] in order to face the problem of precision loss inherent to the Pade approximation.

Finally, the ED-CPT solver is kind of a compromise between the strengths and weaknesses of the Hubbard I and CT-HYB solvers. Like the CT-HYB solver, it avoids truncating the Weiss field. Like the Hubbard I solver, it can work on either the real or the imaginary axis, it does not introduce any stochastic error, and it works well in strongly hybridized problems. The ED-CPT solver does suffer a systematic error caused by bath discretization, when the Weiss field, having the meaning of an infinite bath Green function, is approximated by a model function with a finite number of bath sites. However this problem is mitigated by the use of cluster perturbation theory and is further decreased when using modern HPC computational resources (including GPU cards) which allows the treatment of systems with up to 18 single-orbital sites; this is quite close to the maximum number of sites tractable with exact diagonalization, due to the exponential growth of the Hilbert space with the number of sites [35].

III. EXAMPLES

A. Structural properties of $\gamma - \mathrm{Ce}$

Elemental cerium is well known for having several phases (α, β, γ, δ, α', α'', etc.); for a review, see Ref. [36]. The most puzzling and the most studied phase transition is the $\alpha - \gamma$ isostructural transition, which is accompanied by a 15% volume collapse at room temperature. It is believed that the lattice structure in both α and γ phases is the same (fcc), the lattice constant being the only difference. Within the Mott localization theory of $\alpha - \gamma$ transition in Ce, the transition is viewed as a localization of f electrons in γ phase, while in α phase they remain itinerant [37]. We focus here on γ phase. Its lattice constant is underestimated within LDA by 13% (see below), which is due to the inability of the
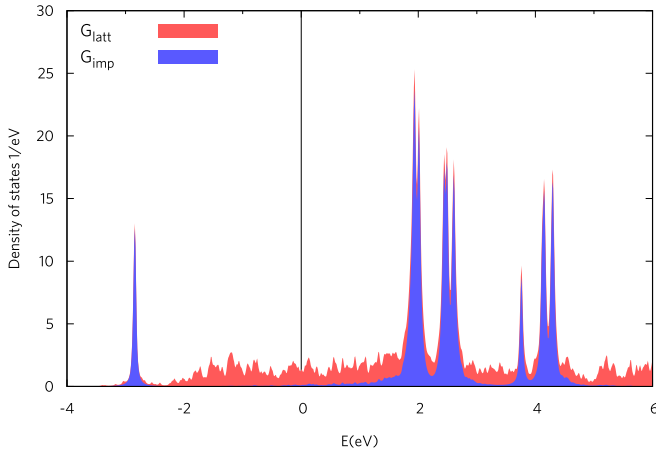
FIG. 2. Density of states of γ-Cerium, calculated by CASTEP's DFT+DMFT implementation and using the Hubbard I impurity solver. G_{imp} labels the impurity Green function derived DOS of Ce f states, and G_{latt} labels the $G^B(k, \omega)$ derived DOS.

FIG. 3. γ-Cerium's total energy E_{tot} as a function of lattice constant a, calculated both with DFT and with DFT+DMFT. Arrows show the experimental, DFT, and DFT+DMFT values of the equilibrium lattice constant. Curves show Birch-Murnaghan fits to the calculated points.

LDA to adequately describe the localization effects. Post-DFT methods such as DFT + U and DFT + DMFT improve the agreement with the experiment, although could not recover 100% of the experimental value [38].

We have used here a $15 \times 15 \times 15$ Monkhorst-Pack k-point mesh [39] (equivalent to k-point spacing of 0.02 Å^{-1}), and the rhombohedral unit cell with $a_{\mathrm{exp}} = 5.161$ Å (experimental value), having a primitive unit cell volume of 34.37 Å^3. For Ce, we have used CASTEP's internally generated scalar relativistic ultrasoft pseudopotential (C9 set) and the following values of Hubbard U and J: $U = 6$ eV and $J = 0.7$ eV. The simulations were carried out at $T = 0.02$ eV. The plane-wave basis cutoff was automatically determined to be 359 eV. In Fig. 2, we report the density of states calculated at the experimental lattice constant a_{exp} using the Hubbard I solver.

It can be clearly seen that the CASTEP+DMFT implementation captures the overall shape of the density of states (DOS) very well as compared to Fig. 5(a) of Ref. [20] and to Ref. [40], while our results appear to be shifted by approximately 0.5 eV, which can be ascribed to the difference in treatment of projections: Namely, we have used the whole energy range of KS eigenstates, as opposed to Refs. [20,40], where an energy window was imposed. The imposition of an energy window implies neglecting the change of the electronic density from the energy regions beyond the window, which may lead to shifts of the chemical potential. In γ-Ce, the application of DMFT leads to the opening of a gap in the f states, being the residual spectral weight due to other orbital moments (d and p states). It is these residual states in the Bloch Green function, strongly dependent on the projection procedure, which eventually determine whether the chemical potential of the insulating system stays at the top of the valence band or at the bottom of the conduction one. Finally, in our calculations there appear extra high energy peaks around 4 eV due to Ce f states as compared to Refs. [20,38]. We have checked that the origin of these peaks is due to a finite Hund's coupling J used in our calculations, as opposed to Refs. [20,38], where $J = 0$ was used.
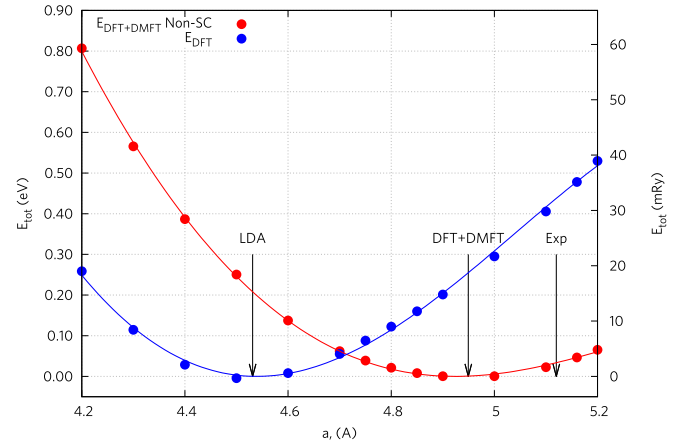
We have also studied the total energy as a function of volume, shown in Fig. 3 and Table I. One can notice a very good qualitative and quantitative agreement of our results with those of Ref. [20]: While the DFT energy minimum is realized at $a = 4.50$ Å (not shown), taking into account the localization effects within DFT+DMFT shifts the minimum to $a = 4.95$ Å, a result slightly closer to the experimental value than that of Ref. [20]. It is interesting to note that among five contributions to the total energy expression, only two are active in the case of Ce, namely the second and the third terms in Eq. (2.9). Indeed, it is argued in Ref. [20] that for the Hubbard I solver applied to Ce f shell, an integer occupation with one electron should be used independently of the lattice constant, and in these circumstances $E_U = 0$, while E^{DC} does not depend on the lattice constant. We remind that everywhere throughout this paper we performed DFT+DMFT calculations with fixed

TABLE I. Comparison of the lattice constant a and bulk modulus B_0 of γ-Ce, Ce$_2$O$_3$, and SmTe calculated within CASTEP's DFT+DMFT implementation with experimental data as well as with theoretical results of Ref. [38].

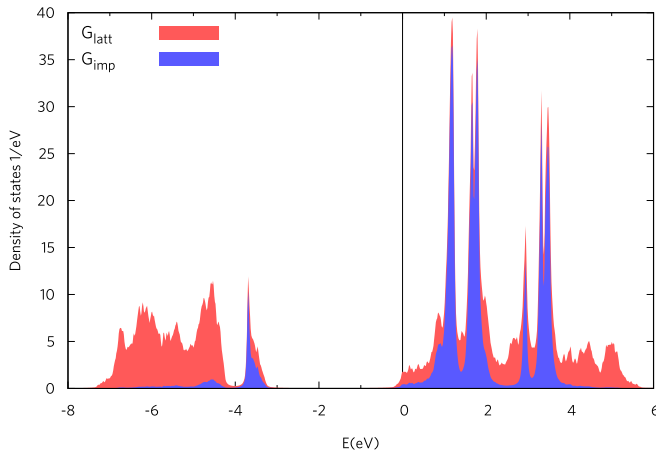| $\gamma -$ **Ce**	a (Å)	B_0 (GPa)
Experiment [38]	5.17	19/21
Present work LDA+DMFT	4.95	30
PAW/LDA+DMFT [38]	4.98	38
ASA/LDA+DMFT [38]	4.91	50
Ce$_2$O$_3$	a (Å)	B_0 (GPa)
Experiment [38]	3.89	111
Present work LDA+DMFT	3.81	164
PAW/LDA+DMFT [38]	3.76	170
ASA/LDA+DMFT [38]	3.79	160
SmTe	a (Å)	B_0 (GPa)
Experiment [26]	6.58	43.5
Present work LDA+DMFT	6.30	54.2
Present work LDA	6.09	65.5

FIG. 4. Density of states of Ce_2O_3 calculated by CASTEP's DFT+DMFT implementation and using the Hubbard I solver. G_{imp} labels the impurity Green function derived DOS of Ce f states, and G_{latt} labels the $G^B(k, \omega)$ derived DOS.

FIG. 5. Ce_2O_3's total energy E_{tot} as a function of lattice constant a, calculated both with DFT and with DFT+DMFT. Arrows show the experimental, DFT, and DFT+DMFT values of the equilibrium lattice constant. Curves show Birch-Murnaghan fits to the calculated data points.

charge. We have applied the fully localized limit (FLL) type of double counting corrections (see Appendix B).

Another structural property which is known to be corrected within DFT+DMFT is the bulk modulus B_0. By fitting the Birch-Murnaghan [41–43] equations of state to the energy versus volume curves of Fig. 3 we obtain an estimate for B_0 which is in line with the predictions of Ref. [38], as shown in Table I. Moreover, even though in general DFT+DMFT systematically overestimates B_0, we can see from Table I that our results are closer to the experimental ones (less overestimating). This is probably because of the difference in the underlying DFT method, as can be seen in Table I, where the results from Ref. [38] for PAW/LDA+DMFT and ASA/LDA+DMFT are clearly different, although the DMFT treatment was identical.

B. Structural properties of cerium sesquioxide

Cerium sesquioxide Ce_2O_3 has been studied for a long time [44–47]. It is known to be an antiferromagnetic insulator with Néel temperature of $T_N = 9$ K and a gap of 2.4 eV. DFT+DMFT calculations in the literature normally address the high-temperature paramagnetic phase, so to benchmark our implementation we also set the temperature to $T = 0.02$ eV. Ce_2O_3 crystallizes in a hexagonal unit cell with space group $P\bar{3}m1$. The experimental parameters for the unit cell are: $a = 3.89$ Å and $c/a = 1.557$, with the Wyckoff positions [48]: Ce $2d$ $(\frac{1}{3}, \frac{2}{3}, 0.24543)$, O $2d$ $(\frac{1}{3}, \frac{2}{3}, 0.6471)$, O $1a$ $(0, 0, 0)$. We have used the same Ce pseudopotential as in the previous subsection, and CASTEP's on-the-fly generated ultrasoft pseudopotential for oxygen (C9 set), and a $17 \times 17 \times 9$ Monkhorst-Pack k-point mesh (equivalent to k-point spacing of approximately 0.02 Å^{-1}). The plane-wave basis cutoff was automatically determined to be 653 eV. The results for Ce_2O_3 density of states at the experimental geometry are shown in Fig. 4 and exhibit excellent agreement with the reference calculations of Ref. [20]. As before, the DMFT calculations were performed with: a Hubbard I solver, and a fixed occupancy of $n = 1$ per Ce atom (in the sense explained
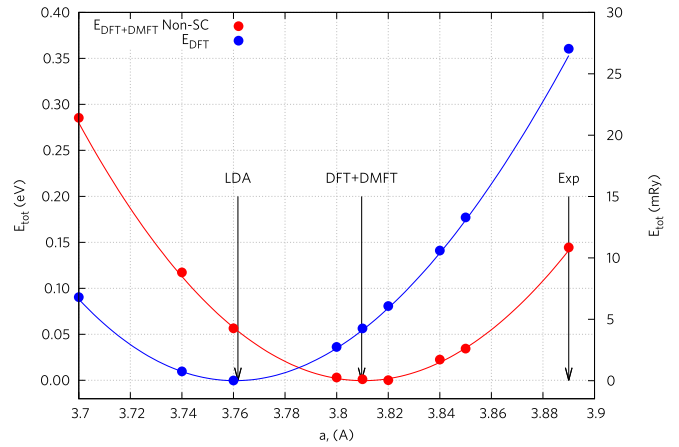
in Ref. [20]) within the FLL double-counting scheme. The result of the application of charge non-self-consistent DMFT in Ce_2O_3 is the opening of a 3 eV gap in the total density of states (while taking into account the charge self-consistency manages to reproduce the experimental gap of 2.4 eV, according to the results of Ref. [20]). The quantitative agreement of our results with those of Ref. [20] is excellent, except for the shift of the chemical potential in the gap, which can be attributed to the difference in the procedure of fixing the total electronic density, as explained in the previous subsection.

The same level of agreement with the reference calculations is exhibited by our total energy calculations, as shown in Fig. 5 and Table I. In doing these calculations, we maintained the ratio c/a as well as the internal positions of the atoms in the unit cell fixed, while changing a. Compared to DFT calculations, which stabilize the unit cell around $a = 3.76$ Å, the DMFT energy minimum is at a larger value of 3.81 Å, which is very close to the results of Refs. [20,38]. Moreover, our result for the lattice constant a is somewhat closer to the experimental value, while our B_0 is between the two results of Ref. [38].

C. Structural properties of SmTe

In order to demonstrate the capabilities of the implementation further, we apply it to a study of the equation of state of samarium telluride (SmTe). We have used here a $19 \times 19 \times 19$ Monkhorst-Pack k-point mesh [39] (equivalent to k-point spacing of 0.02 Å^{-1}), and the face-centered cubic unit cell with two atoms [Sm at $(0,0,0)$ and Te at $(\frac{1}{2}, \frac{1}{2}, \frac{1}{2})$]. We have scanned the values of cubic lattice constants from $a = 5.5$ Å to $a = 6.8$ Å. For f electrons on Sm, we have used $U = 6.1$ eV and $J = 0.835$ eV. For Sm and Te, we have used CASTEP's internally generated scalar relativistic ultrasoft pseudopotentials (C9 set). The plane-wave basis cutoff was 425 eV.

In Fig. 6, we report the density of states calculated at the value of a corresponding to a minimum of E_{tot} within DFT+DMFT ($a_{DMFT} = 6.3$ Å) using the Hubbard I solver.
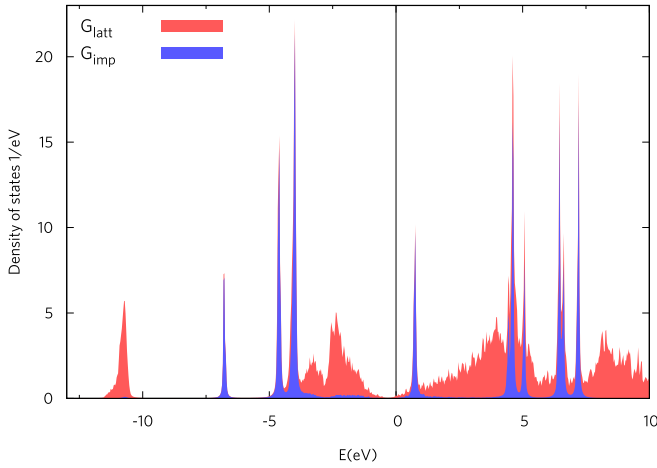
FIG. 6. Density of states of SmTe calculated by CASTEP's DFT+DMFT implementation and using the Hubbard I solver. G_{imp} labels the impurity Green function derived DOS of Sm f states, and G_{latt} labels the $G^B(\mathbf{k}, \omega)$ derived DOS.

It can be seen that the effect of improved treatment of the electronic correlations of f electrons on Sm is to open a gap in the f states and to remove them from the Fermi level, so that the system becomes a semiconductor in accordance with the experimental findings [26].

Standard LDA underestimates the equilibrium lattice constant of SmTe due to its inability to properly treat the Sm f-orbitals' localization, as can be seen from Fig. 7. Inclusion of the localization effects within our DFT+DMFT implementation increases the equilibrium a. The improvement with respect to LDA is as follows: LDA mismatch is 7%, while DFT+DMFT mismatch is 4%. The same type of improvement is observed for bulk modulus as can be seen from Table I: LDA overestimates B_0 by 51%, while the DFT+DMFT estimate is closer to the experimental value (25% of error). It is evident that our implementation of DFT+DMFT significantly improves the
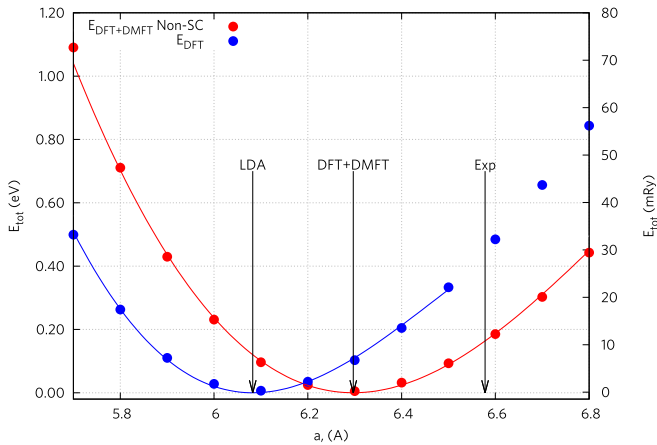

FIG. 7. SmTe's total energy E_{tot} as a function of lattice constant a, calculated both with DFT and with DFT+DMFT. Arrows show the experimental, DFT, and DFT+DMFT values of the equilibrium lattice constant. Curves show Birch-Murnaghan fits to the calculated data points.
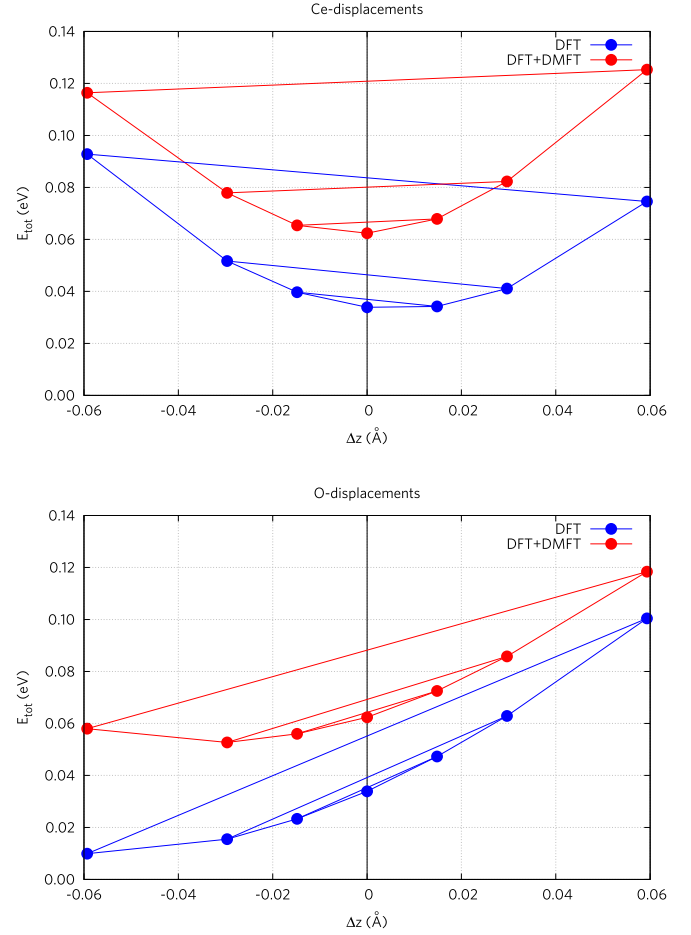

FIG. 8. The total energy as a function of the z-position increments Δz of Ce (upper panel) and oxygen (lower panel) for three different increments: $\Delta z = 4\%$, 2%, 1% in units of c-axis lattice spacing. a was kept equal to 3.81 Å. The energies are shifted in order to fit the graph.

agreement of strongly correlated materials simulations with the experiment.

IV. CALCULATION OF FORCES IN CERIUM SESQUIOXIDE

In order to understand better the discrepancy between DFT+DMFT and the experimental lattice constants in Ce_2O_3, we proceed to calculate the atomic forces. For that purpose, we first note that most internal atomic coordinates are fixed by symmetry. We vary the remaining coordinates, which are the z coordinates of Ce $2d$ and O $2d$ atoms (the ones established from experiment). Obviously, the forces of the atoms related by symmetry are in turn related. During finite increment of relevant atomic coordinates, we tested several Δz values, in order to be sure that the total energy varies linearly over the length scale of Δz. The results of these tests are shown in Fig. 8, where we report the total energy profile for three different values of Δz: 4%, 2%, 1% in units of the c dimension of the unit cell. To ease the comparison, we added thin lines, whose slope indicates the forces (up to the minus sign):

$$F_{z_i} = -\frac{\partial E_{\text{tot}}}{\partial z_i}.$$

TABLE II. Atomic forces on Ce_2O_3's Ce $2d$ and O $2d$ atoms, in units of eV/Å. The forces are calculated both with DFT and with DFT+DMFT at two values of the lattice constant: the experimental value $a = 3.89$ Å and the value predicted by DFT+DMFT $a = 3.81$ Å.

	DFT		DFT+DMFT	
	$a = 3.81$ Å	$a = 3.89$ Å	$a = 3.81$ Å	$a = 3.89$ Å
Ce	0.09	0.46	-0.04	0.35
O	-0.40	-0.30	-0.28	-0.17

It can be seen from Fig. 8 that the slope remains almost independent of Δz, therefore, in the following we use $\Delta z = 1\%$. Table II summarizes our results for the atomic force calculations of Ce_2O_3. In addition, we emphasise that the total energy as a function of Δz is a smooth differentiable function, thanks to the fact that both DFT (CASTEP) and DMFT subsystems in our calculations are well behaved, giving small responses to small perturbations. Moreover, CASTEP DFT, being a plane-wave code, does not introduce Pulay forces. We have performed calculations for two lattice constants $a = 3.81$ Å (minimum energy for DFT+DMFT method) and $a = 3.89$ Å (the experimental value), while the ratio c/a was kept fixed at the experimental value $c/a = 1.557$. We notice that taking into account strong correlations of Ce f shells within DMFT shows a systematic decrease of the forces with respect to DFT, as illustrated in Fig. 9. This is the consequence of stronger cerium f-electron charge localization predicted by DMFT as compared to DFT, so that these electrons participate less in formation of covalent bonds with oxygen. This argument remains valid even though in our calculations the electronic density is fixed: The total energy will be lower at larger volumes in DMFT.

V. CONCLUSIONS

In conclusion, we have performed thorough DFT+DMFT studies of bulk properties in γ-Ce, Ce_2O_3 and SmTe including bulk modulus, equilibrium volume, forces, and spectral weight. We have used a DFT+DMFT formalism in the plane-wave code CASTEP, for which case we rederived all the necessary formulas. We have made a comparison of our results with the
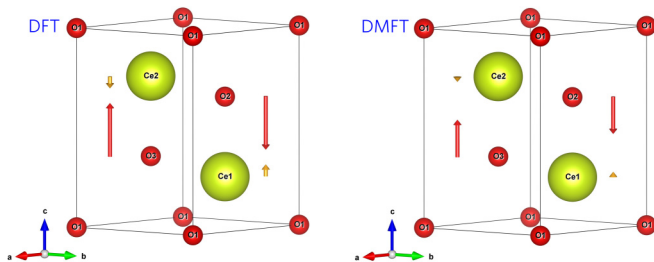
FIG. 9. A graphical comparison of forces calculated at the lattice constant $a = 3.81$ Å within DFT (left panel) and DFT+DMFT (right panel). Forces acting on $Ce_{1(2)}$ and $O_{2(3)}$ atoms are shown. The lengths of arrow are proportional to the forces. Notice much smaller forces in the case of DMFT.

ones available from literature. The overall agreement of our spectral weight with the reference publication of Ref. [20] is very good, taking into account the difference in procedure employed to fix the chemical potential. Our predicted bulk modulus somewhat better agrees with the experiment than what was previously published because of very well controlled underlying DFT description given by CASTEP. The same can be said about the equilibrium volume (compared with the non-SC results of Ref. [20]): Our equilibrium volume for γ-Ce lays in between PAW/LDA+DMFT and ASA/LDA+DMFT of Ref. [38], while for Ce_2O_3 our results are closer to ASA/LDA+DMFT. The general effect of applying DFT+DMFT on all the systems considered here is to increase the localization of the f electrons with respect to DFT treatment, which leads to larger estimates for equilibrium volumes. In addition, we have also studied SmTe's equation of state and demonstrated that improved treatment of strong localization effects within DFT+DMFT improves the agreement with the experiment as compared to LDA. To understand why DFT+DMFT does not fully recover the equilibrium volume in Ce_2O_3, we performed the internal forces calculations corresponding to the coordinates not constrained by symmetry. Our results show that within the more realistic DFT+DMFT treatment, the atomic forces in cerium sesquioxide appear to be profoundly different from the DFT ones.

A further point of novelty in our implementation is the ability to work equally well both with norm-conserving and ultrasoft pseudopotentials, since we accounted for the localized basis nonorthogonality via introduction of scalar product metric. This approach could be of interest when dealing with DMFT within, e.g., PAW formalism or any other formalism, which uses nonorthogonal basis.

APPENDIX A: DETAILS OF COULOMB INTERACTION TREATMENT

In the Hubbard-I solver, we use the most general form of Coulomb interaction vertex (4-index):

$$H_{ee} = \frac{1}{2} \sum U(m_1, m_2, m_3, m_4) c^{\dagger}_{lm_1,\sigma} c^{\dagger}_{lm_2,\sigma'} c_{lm_4,\sigma'} c_{lm_3,\sigma}.$$

Internally, in the solver, in order to have a rough estimate of the ground state sector, we have also used the reduced Coulomb interaction vertex with two indices:

$$H_{ee} = \frac{1}{2} \sum U^{\sigma,\sigma'}_{m_1,m_2} n_{lm_1,\sigma} n_{lm_2,\sigma'}. \tag{A1}$$

Here the Coulomb matrix elements are expressed through $U(m_1, m_2, m_3, m_4)$ as follows:

$$U_{m_1,m_2}^{\uparrow\uparrow} = U_{m_1,m_2}^{\downarrow\downarrow} = U(m_1, m_2, m_1, m_2) - U(m_1, m_2, m_2, m_1)$$

$$U_{m_1,m_2}^{\uparrow\downarrow} = U_{m_1,m_2}^{\downarrow\uparrow} = U(m_1, m_2, m_1, m_2).$$

Coulomb matrix elements $U(m_1, m_2, m_3, m_4)$ can be expressed through the Slater integrals $F(n)$, assuming the spherical approximation [20]:

$$U(m_1, m_2, m_3, m_4) = \sum_{k=0}^{l} F(2k) \frac{4\pi}{2k+1} \sum_{q=-k}^{k} \langle lm_1|Y_{kq}|lm_3 \rangle \langle lm_2|Y_{kq}^{\star}|lm_4 \rangle$$

$$= \sum_{k=0}^{l} F(2k)(2l+1)^2 \begin{pmatrix} l & k & l \\ 0 & 0 & 0 \end{pmatrix}^2 \sum_{q=-k}^{k} (-1)^{m_1+m_2+q} \begin{pmatrix} l & k & l \\ -m_1 & q & m_3 \end{pmatrix} \begin{pmatrix} l & k & l \\ -m_2 & -q & m_4 \end{pmatrix}, \quad \text{(A2)}$$

where $\begin{pmatrix} j_1 & j_2 & j_3 \\ m_1 & m_2 & m_3 \end{pmatrix}$ are Wigner $3j$ symbols, while Y_{kq} are spherical harmonics. We report for completeness the relations among Slater integrals and U and J for d and f orbitals.

For d orbitals with $l = 2$, $2k$ in (A2) runs from 0 to 4 taking even values:

$$F(0) = U$$

$$F(2) = \frac{14J}{1.625}$$

$$F(4) = 0.625 F(2).$$

For f orbitals with $l = 3$ there is one more term $F(6)$, while $F(2)$ and $F(4)$ are different with respect to the previous case:

$$F(0) = U$$

$$F(2) = \frac{6435J}{286 + \frac{195 \times 451}{675} + \frac{250 \times 1001}{2025}}$$

$$F(4) = \frac{451}{675} J$$

$$F(6) = \frac{1001}{2025} F(2).$$

APPENDIX B: DOUBLE COUNTING CORRECTION SCHEMES

The double counting problem arises in both DFT+U and DFT+DMFT methods since the amount of correlations present at the DFT level and originating from the density functional is unknown. In order not to count the same amount of correlations twice at both DFT and DMFT levels, we need to adopt some model for DFT correlations and subtract this double counting potential V_σ^{DC} from the lattice Green function. There are several approaches to this problem [49–54]. In CASTEP, we implement the following types of the double counting corrections: (i) Fully localized limit (FLL), (ii) around mean-field limit (AMF) [49–51], and (iii) Held's mean-field one [52]. The expressions for the double-counting energy E_{DC} and the double-counting potential V_σ^{DC} are reported below.

(1) FLL: In this approximation, it is assumed that the occupation $n_{m\sigma}$ of an orbital m, σ can be either 0 or 1. We denote $N_\sigma = \sum_m n_{m\sigma}$ and $N_{\text{tot}} = \sum_\sigma N_\sigma$. Then, from (A1)

and assuming that $U_{m_1,m_2}^{\sigma,\sigma'} = U$ is constant, we arrive at:

$$E_{DC} = \frac{1}{2} U N_{\text{tot}}(N_{\text{tot}} - 1) - \frac{1}{2} J \sum_\sigma N_\sigma(N_\sigma - 1).$$

The double counting potential can be obtained by differentiating E_{DC} with respect to N_σ

$$V_\sigma^{DC} = U\left(N_{\text{tot}} - \tfrac{1}{2}\right) - J\left(N_\sigma - \tfrac{1}{2}\right).$$

We note that the above formulas remain valid also in the case when $U_{m_1,m_2}^{\sigma,\sigma'}$ and J are orbital dependent [50]. In that case, U has the meaning of averaged Coulomb interaction. It is assumed within FLL that the electrons are fully localized, hence it is normally suited to model insulating systems.

(2) AMF: This is the opposite limit, where it is assumed that an average occupation $n_{m\sigma}$ of an orbital m, σ is independent on m, so that

$$n_{m\sigma} = n_\sigma \equiv \frac{N_\sigma}{2l+1},$$

where N_σ is the total occupation of the impurity site in the spin channel σ and with l orbitals. After some simplifications we arrive at:

$$E_{DC} = U N_\downarrow N_\uparrow + \frac{2l}{2l+1} \frac{(U-J)}{2} (N_\uparrow^2 + N_\downarrow^2)$$

$$V_\sigma^{DC} = U\left(N_{\text{tot}} - \frac{N_\sigma}{2l+1}\right) - J N_\sigma\left(\frac{2l}{2l+1}\right).$$

This is somehow the opposite to the FLL case and it is normally applied to metals.

(3) Held's formula: Average Coulomb repulsion $\overline{U}$ is introduced in order to ensure the rotational invariance as follows:

$$\overline{U} = \frac{U + (l-1)(U-2J) + (l-1)(U-3J)}{2l-1}.$$

Here l is the degeneracy of the shell. The E_{DC} and V_σ^{DC} are then expressed as:

$$E_{DC} = \frac{\overline{U} N_{\text{tot}}(N_{\text{tot}} - 1)}{2}$$

$$V_\sigma^{DC} = \overline{U}\left(N_{\text{tot}} - \frac{1}{2}\right).$$

APPENDIX C: MATSUBARA FREQUENCY SUMMATIONS

We derive here an alternative form of Green function high-frequency tails in Matsubara representation. We start by defining the spectral moment expansion of the Green function up to the lth moment:

$$G(i\omega_n) = \frac{a_1}{i\omega_n} + \frac{a_2}{(i\omega_n)^2} + \frac{a_3}{(i\omega_n)^3} + \ldots + \frac{a_l}{(i\omega_n)^l}. \quad \text{(C1)}$$

Here we assume G and $\{a_i\}$ to be matrices. We assume that $\{a_i\}$ are obtained, e.g., by fitting the numerical data or by analytical calculations of Hamiltonian commutators. As usual, we decompose the Green function into G^{num} given by a numerical solution of the impurity problem and defined up to a Matsubara frequency $\omega_{\text{max}} = \pi T(2n_{\text{max}} + 1)$, and $G^{\text{an}}(i\omega) = \sum_m \frac{a_m}{(i\omega)^m}$, defined for all Matsubara frequencies. We then sum numerically

$$S_1 = T \sum_{n=-n_{\text{max}}-1}^{n_{\text{max}}} (G^{\text{num}}(i\omega_n) - G^{\text{an}}(i\omega_n))$$

and separately, analytically, $S_2 = T \sum_n G^{\text{an}}(i\omega_n)$. The final result can be written as:

$$T \sum_n G(i\omega_n) e^{i\omega_n 0^+} \approx S_1 + S_2.$$

We note that the sums here are extended over both positive and negative Matsubara frequencies, and, hence, odd powers of $i\omega$ do not contribute to S_2 (but must be included in S_1). We report below the analytical formulas for even power contributions to G^{an} up to eighth order. The coefficient $e^{i\omega_n 0^+}$ is implied in order to ensure the convergence:

$$T \sum_{i\omega_n} \frac{1}{i\omega_n} = \frac{1}{2}$$

$$T \sum_{i\omega_n} \frac{1}{(i\omega_n)^2} = -\frac{1}{4T}$$

$$T \sum_{i\omega_n} \frac{1}{(i\omega_n)^4} = \frac{1}{48T^3} \quad \text{(C2)}$$

$$T \sum_{i\omega_n} \frac{1}{(i\omega_n)^6} = -\frac{1}{480T^5}$$

$$T \sum_{i\omega_n} \frac{1}{(i\omega_n)^8} = \frac{17}{80640T^7}.$$

Calculation of the correlation energy within the Galitskii-Migdal formula (2.10) can be, in principle, done in the same manner. One only needs to express the tails of the product

in terms of the multipliers' tails. However, we find it more convenient to rewrite the formula in another form, using the Dyson equation: $G_0^{-1} = G^{-1} + \Sigma$, so that only the tails of G are involved:

$$E_{\text{corr}} = \frac{T}{2}\text{Tr}\Sigma_n G(i\omega_n)\Sigma(i\omega_n)$$

$$= \frac{T}{2}\text{Tr}\Sigma_n \left(G_0^{-1}(i\omega_n)G(i\omega_n) - 1\right).$$

G_0 has a very simple form by construction. Moreover, G_0^{-1} is at most a linear function of complex frequency:

$$G_0^{-1}(i\omega_n) = i\omega_n - \varepsilon_0.$$

As above, we split E_{corr} into E_{num} and E_{an}:

$$E_{\text{corr}} = E_{\text{num}} + E_{an},$$

where

$$E_{\text{num}} = \frac{T}{2}\text{Tr} \sum_{n=-n_{\text{max}}-1}^{n_{\text{max}}} (i\omega_n - \varepsilon_0)(G(i\omega_n) - G^{\text{an}}(i\omega_n))$$

and

$$E^{\text{an}} = \frac{T}{2} \sum_{\omega_n} \left\{ \sum_{l=1}^{N-1} \frac{\text{Tr}(a_{l+1} - a_l \times \varepsilon_0)}{(i\omega_l)^l} + \frac{\text{Tr}(a_N \times \varepsilon_0)}{(i\omega_n)^N} \right\}, \quad \text{(C3)}$$

where $G^{\text{an}}(i\omega_n)$ is given by (C1). By using formulae (C2), in (C3), we arrive at:

$$E^{\text{an}} = \frac{1}{2}\left\{ \frac{1}{2}(\text{Tr}(a_2 - a_1 \times \varepsilon_0) - \frac{1}{4T}(\text{Tr}(a_3 - a_2 \times \varepsilon_0) + \frac{1}{48T^3}(\text{Tr}(a_5 - a_4 \times \varepsilon_0) + \ldots \right\}.$$

We remind that here $\{a_i\}$ and ε_0 are matrices, Tr is the usual trace operation on matrix, while "$\times$" stands for matrix-matrix product. The advantage of this method stays in the fact that we do not require the spectral moments of the self-energy (which could be of worse quality), while the expansion can be easily extended up to an arbitrary power of $i\omega$. This calculation scheme is especially useful, when using quantum Monte Carlo solvers, in which there is an intrinsic bias in determination of high-frequency tails. In our calculations, we used l between 5 and 7, which allowed us to have a typical round-off error on correlation energy around 10^{-6} eV at a typical temperature of $T = 0.02$ eV, as compared to an independently calculated value.

[1] P. Hohenberg and W. Kohn, Phys. Rev. **136**, B864 (1964).

[2] W. Kohn and L. J. Sham, Phys. Rev. **140**, A1133 (1965).

[3] R. O. Jones, Rev. Mod. Phys. **87**, 897 (2015).

[4] G. Kotliar and D. Vollhardt, Phys. Today **57**(3), 53 (2004).

[5] C. Weber, D. D. O'Regan, N. D. M. Hine, M. C. Payne, G. Kotliar, and P. B. Littlewood, Phys. Rev. Lett. **108**, 256402 (2012).

[6] C. Weber, D. D. O'Regan, N. D. M. Hine, P. B. Littlewood, G. Kotliar, and M. C. Payne, Phys. Rev. Lett. **110**, 106402 (2013).

[7] E. Plekhanov, S. Sorella, and M. Fabrizio, Phys. Rev. Lett. **90**, 187004 (2003).

[8] E. Plekhanov, F. Becca, and S. Sorella, Phys. Rev. B **71**, 064511 (2005).

[9] P. Dai, Rev. Mod. Phys. **87**, 855 (2015).

[10] L. K. Joy, S. S. Samatham, S. Thomas, V. Ganesan, S. Al-Harthi, A. Liebig, M. Albrecht, and M. R. Anantharaman, J. Appl. Phys. **116**, 213701 (2014).

[11] S. Babulanam, T. Eriksson, G. Niklasson, and C. Granqvist, Sol. Energy Mater. **16**, 347 (1987).

[12] C. Granqvist, Thin Solid Films **193-194**, 730 (1990).

[13] C. G. Granqvist, Sol. Energy Mater. Sol. Cells **91**, 1529 (2007).

[14] J. M. Tomczak and S. Biermann, Europhys. Lett. **86**, 37004 (2009).

[15] A. Georges, G. Kotliar, W. Krauth, and M. J. Rozenberg, Rev. Mod. Phys. **68**, 13 (1996).

[16] D. Vollhardt, AIP Conf. Proc. **1297**, 339 (2010).

[17] S. Y. Savrasov and G. Kotliar, Phys. Rev. B **69**, 245101 (2004).

[18] J. Minár, L. Chioncel, A. Perlov, H. Ebert, M. I. Katsnelson, and A. I. Lichtenstein, Phys. Rev. B **72**, 045125 (2005).

[19] G. Kotliar, S. Y. Savrasov, K. Haule, V. S. Oudovenko, O. Parcollet, and C. A. Marianetti, Rev. Mod. Phys. **78**, 865 (2006).

[20] L. V. Pourovskii, B. Amadon, S. Biermann, and A. Georges, Phys. Rev. B **76**, 235101 (2007).

[21] M. C. Payne, M. P. Teter, D. C. Allan, T. Arias, and J. D. Joannopoulos, Rev. Mod. Phys. **64**, 1045 (1992).

[22] S. J. Clark, M. D. Segall, C. J. Pickard, P. J. Hasnip, M. J. Probert, K. Refson, and M. Payne, Z. Kristall. **220**, 567 (2005).

[23] B. Amadon, F. Lechermann, A. Georges, F. Jollet, T. O. Wehling, and A. I. Lichtenstein, Phys. Rev. B **77**, 205112 (2008).

[24] A. I. Lichtenstein, Electronic structure of complex oxides, in *Spintronics: From Materials to Devices*, edited by C. Felser and G. H. Fecher (Springer, Netherlands, 2013), p. 167.

[25] F. Lechermann, A. Georges, A. Poteryaev, S. Biermann, M. Posternak, A. Yamasaki, and O. K. Andersen, Phys. Rev. B **74**, 125120 (2006).

[26] U. Benedict and W. Holzapfel, in *Lanthanides/Actinides: Physics I*, edited by K. A. Gschneidner, Jr., L. Eyring, G. H. Lander, and G. R. Choppin, Handbook on the Physics and Chemistry of Rare Earth, Vol. 17 (Elsevier, Amsterdam, 1993), p. 245.

[27] V. Galitskii and A. Migdal, JETP **7**, 96 (1958).

[28] B. Russell, M. Payne, and L. C. Ciacchi, Phys. Rev. B **79**, 165101 (2009).

[29] R. M. Martin, *Electronic Structure: Basic Theory and Practical Methods* (Cambridge University Press, Cambridge, 2004).

[30] J. Hubbard, Proc. R. Soc. London, Ser. A **276**, 238 (1963).

[31] O. Parcollet, M. Ferrero, T. Ayral, H. Hafermann, I. Krivenko, L. Messio, and P. Seth, Comput. Phys. Commun. **196**, 398 (2015).

[32] C. Weber, A. Amaricci, M. Capone, and P. B. Littlewood, Phys. Rev. B **86**, 115136 (2012).

[33] H. J. Vidberg and J. W. Serene, J. Low Temp. Phys. **29**, 179 (1977).

[34] D. M. Smith, ACM Trans. Math. Softw. **17**, 273 (1991).

[35] E. Koch, in *DMFT at 25: Infinite Dimensions*, edited by E. Pavarini, E. Koch, D. Vollhardt, and A. Lichtenstein (Forschungszentrum Jülich Zentralbibliothek, Verlag, Jülich, 2014), Chap. 8.

[36] A. V. Nikolaev and A. V. Tsvyashchenko, Phys.-Usp. **55**, 657 (2012).

[37] N. Devaux, M. Casula, F. Decremps, and S. Sorella, Phys. Rev. B **91**, 081101 (2015).

[38] B. Amadon, J. Phys.: Condens. Matter **24**, 075604 (2012).

[39] H. J. Monkhorst and J. D. Pack, Phys. Rev. B **13**, 5188 (1976).

[40] TRIQS tutorial, Ce with Hubbard-I approximation.

[41] F. D. Murnaghan, Proc. Natl. Acad. Sci. USA **30**, 244 (1944).

[42] F. Birch, Phys. Rev. **71**, 809 (1947).

[43] M. Hebbache and M. Zemzemi, Phys. Rev. B **70**, 224107 (2004).

[44] D. A. Andersson, S. I. Simak, B. Johansson, I. A. Abrikosov, and N. V. Skorodumova, Phys. Rev. B **75**, 035109 (2007).

[45] S. Fabris, S. de Gironcoli, S. Baroni, G. Vicario, and G. Balducci, Phys. Rev. B **71**, 041102 (2005).

[46] N. Singh, S. M. Saini, T. Nautiyal, and S. Auluck, J. Appl. Phys. **100**, 083525 (2006).

[47] C. Loschen, J. Carrasco, K. M. Neyman, and F. Illas, Phys. Rev. B **75**, 035115 (2007).

[48] R. W. G. Wyckoff, *Crystal Structures*, 2nd ed. (Interscience, New York, 1967), Vol. 2, p. 1.

[49] V. I. Anisimov, J. Zaanen, and O. K. Andersen, Phys. Rev. B **44**, 943 (1991).

[50] M. T. Czyżyk and G. A. Sawatzky, Phys. Rev. B **49**, 14211 (1994).

[51] M. Karolak, G. Ulm, T. Wehling, V. Mazurenko, A. Poteryaev, and A. Lichtenstein, J. Electron. Spectrosc. Relat. Phenom. **181**, 11 (2010).

[52] K. Held, Adv. Phys. **56**, 829 (2007).

[53] K. Haule, Phys. Rev. Lett. **115**, 196403 (2015).

[54] H. Park, A. J. Millis, and C. A. Marianetti, Phys. Rev. B **90**, 235103 (2014).